J. Fluid Mech. (2002), *vol.* 459, *pp.* 245–276.
DOI: 10.1017/S002211200200798X Printed in the United Kingdom

Electric measurements of charged sprays emitted by cone-jets

By MANUEL GAMERO-CASTAÑO† AND VLADIMIR HRUBY

Busek Co. Inc., 11 Tech Circle, Natick, MA 01760, USA

(Received 26 March 2001 and in revised form 15 November 2001)

We use time-of-flight and energy analysis techniques to measure in a vacuum the charge, specific charge and stopping potential of primary and satellite droplets generated by electrosprays of tributyl phosphate solutions. This information, of interest in itself, is subsequently analysed to obtain the following relevant parameters of the jet emanating from the Taylor cone: the velocity of the fluid at the breakup point, the voltage difference between the liquid cone and jet breakup location, and the most probable wavelength for varicose breakup. A large fraction of the electrospray needle voltage is used to accelerate the jet. Indeed, for the solutions of lowest electrical conductivities studied here, the voltage difference between electrospray needle and jet breakup location becomes approximately 90% of the needle voltage. In addition, the pressure of the jet fluid at the breakup point is negligible compared to its specific kinetic energy. The specific charge distribution function of the main droplets produced in the varicose breakup is remarkably narrow. Hence, the limiting and commonly accepted case of varicose breakup at constant electric potential is not consistent with this experimental observation. On the other hand, a scenario in which the electric charge is bound to the jet surface seems to be a good approximation to simulate the effect of charge on capillary breakup. It is also found that the effect of viscosity on the formation of droplets is paramount in electrosprays of moderate and high electrical conductivity. We expect that these measurements will guide the analytical modelling of cone-jets.

1. Introduction

The use of moderate electric fields to generate charged liquid droplets is a well-documented practice. This technique is referred to as electrospray. Its ability to produce beams of relatively monodisperse droplets with diameters as small as a few nanometres is unmatched by other spraying methods. Electrospray is a most familiar tool in the field of mass spectrometry (Fenn *et al.* 1989), as documented by the more than one thousand research articles written every year on this subject. Other areas of interest include electrostatic printing, nanoparticle technology and electric propulsion (Huberman & Rosen 1974; Lenggoro *et al.* 2000; Gamero-Castaño & Hruby 2001). The wide range of applications in which electrospray has proved useful has motivated, especially during the last decade, a significant amount of activity aimed at studying this phenomenon. In a typical experimental configuration, a liquid flow is fed through a capillary needle, and a voltage difference between needle and a facing electrode

† Author to whom all correspondence should be addressed.

is set. If the voltage difference and flow rate are adequate, a stable liquid meniscus (Taylor cone) with a slender jet issuing from its apex is formed. Eventually, the jet becomes unstable and breaks up, generating a spray of charged droplets. Due to the geometric resemblance, the type of electrospray studied in this article is known as the cone-jet mode (Cloupeau & Prunet-Foch 1990).

Despite the vast quantity of experimental data that appears in the scientific literature, few characteristics of the electrospraying process have been measured. This has contributed to the proliferation of alternative models and theories aimed to explain the behaviour of electrosprays. Although the complete set of differential equations and boundary conditions that determine the dynamics of a cone-jet are well known (Saville 1997), the complexity of this problem (disparity of length scales, complex geometry with a free surface, time dependence of the jet breakup region, etc.) is such that simplifying hypotheses need to be adopted in order to attempt analytical or numerical solutions. However, because of insufficient experimental insight, models based on competing hypotheses are found side by side in the literature (Fernández de la Mora & Loscertales 1994; Gañán-Calvo 1997*a*). This confusion is further aggravated by the fact that the existing experimental measurements do not suffice to either completely support or reject some of these models. Hence, it is clear that the electrospray community will greatly benefit from the measurement of additional and meaningful electrohydrodynamic quantities. The first explanation for the lack of a diverse set of experimental data is that the accurate measurement of most fluid-dynamic and electric variables of jets of submicrometric dimensions is difficult. A second, more subtle contributing reason is that, although a varied phenomenology associated with the electrospraying process can be recorded, the lack of theoretical knowledge about the overall problem makes it difficult to translate this phenomenology into well-defined electro-fluid-dynamic parameters.

Let us illustrate the above statements with some examples. The electric current emitted by the cone-jet is its characteristic most frequently reported (Fernández de la Mora & Loscertales 1994; Chen & Pui 1997; Gañán-Calvo, Dávila & Barrero 1997). Typically, it is compiled as a function of flow rate and physical properties of the sprayed solution, and accurate measurement does not require excessive effort. Although the electric current is a main property of the electrospraying process, it is not a differentiating one: the leading and competing electrospray models predict the same functional relation for the electric current (Fernández de la Mora & Loscertales 1994; Gañán-Calvo 1997*a*; Cherney 1999).

The diameter of electrospray droplets can be measured with a variety of diagnostic tools such as phase Doppler anemometers, aerodynamic size spectrometers, etc. (Rosell-Llompart & Fernández de la Mora 1994; Tang & Gomez 1994; Gañán-Calvo *et al.* 1997). Most of these techniques use optical detectors, and thus are limited to the measurement of droplets larger than a few tenths of a micron. Furthermore the droplet diameter cannot be regarded as a primary characteristic of the cone-jet itself: it is well known that, at fixed conditions, an electrified liquid jet generates a cloud of droplets of varying size, and that several parameters related to the breakup process determine the mean diameter of the distribution. Furthermore, although electrospray models yield functional forms for the droplet diameter, or more properly for the characteristic diameter of the jet, the differences between the predictions of conflicting models are comparable to the accuracy with which droplets can be experimentally sized. Thus, the same experimental data seem to fit different theories equally well.

The diameters of electrified jets are measured in several studies by means of high resolution cameras (Gañán-Calvo 1997*b*). Only jets with diameters larger than a few

microns can be studied in this manner, with a poor resolution in the micron range. The quality of these measurements worsens when the analysed region approaches the breakup zone, due to the high frequencies at which the jet evolves. Tang & Gomez (1994) have succeeded in photographing the breakup region of heptane cone-jets. For these relatively thick jets (roughly 15 μm jet diameter), they measure a value of 1.9 for the ratio between the radii of main droplets and jet. This number is in agreement with the value of 1.89 derived by Lord Rayleigh (1945) in his classical instability analysis of inviscid and uncharged, capillary jets.

There are very few cases in which both the diameter and the charge of submicron electrospray droplets are measured (see Javorek & Krupa 1996 for supermicron jets). De Juan & Fernández de la Mora (1997) use an experimental technique featuring a differential mobility analyser and an aerodynamic size spectrometer in tandem to measure the charge and size of droplets. Among other results, they find that the distribution function for the droplet specific charge is narrower than the diameter distribution. In the electrosprays studied by de Juan & Fernández de la Mora (1997), the fact that the specific charge of the fluid remains approximately constant during the breakup reveals two important qualities: first, most of the electric current in the final region of the jet must move in the form of convected surface charge, rather than being conduction current; second, the breakup time must be much shorter than the time required for an efficient redistribution of surface charge. This experimental finding is in contradiction with the equipotential breakup hypothesis proposed by several researchers (López-Herrera, Gañán-Calvo & Pérez-Saborid 1999; Hartman *et al.* 2000).

Finally, the measurement of the rate at which ions are field emitted from the surface of the cone-jet can be used to estimate the maximum electric field normal to the jet surface (Gamero-Castaño & Fernández de la Mora 2000). However, the study of a difficult problem such as electrospray through the more complex ion field evaporation phenomena is, to say the least, a rather complicated task.

In this article we use stopping potential and time-of-flight techniques in electrosprays containing primary and satellite droplets to measure the jet velocity and diameter at its breakup point, its voltage with respect to the needle supporting the cone-jet, the charge and diameter of individual droplets, and the most probable wavelength for varicose breakup. The structure of the paper is as follows: after this introductory section we describe the experimental arrangement, liquid solutions and diagnostic techniques. We will briefly explain the fundamentals of the time-of-flight and stopping-potential analysis. A detector used to measure both the charge and specific charge of individual droplets is described in detail. The discussion of the main experimental findings is given in § 3. This section is divided in two parts: in the first we list and analyse the measurements of the voltage drop along the cone-jet and the diameter of the jet at the breakup point; in the second we take advantage of the information yielded by the distribution functions of the specific charge of the droplets to obtain conclusions about the jet breakup process, we solve a model of varicose breakup in which the effect of surface charge is retained, and compare the model's predictions for the ratio between droplet and jet diameter with experimental measurements. The article then ends with some brief conclusions.

2. Experimental

We have studied five solutions of tributyl phosphate, TBP, with electrical conductivities ranging from $2.3 \times 10^{-4}\,\mathrm{S\,m^{-1}}$ to $2.2 \times 10^{-2}\,\mathrm{S\,m^{-1}}$. This liquid (Alfa Aesar

Solution	Solute	Solute conc. (% wt)	K (S m^{-1})
TBP1	Emi-Im	2.9	2.20×10^{-2}
TBP2	TBTP	1.5	8.53×10^{-3}
TBP3	TBTP	0.15	1.64×10^{-3}
TBP4	TBTP	0.050	5.34×10^{-4}
TBP5	TBTP	0.015	2.30×10^{-4}

TABLE 1. Composition and electrical conductivity of the solutions electrosprayed. Emi-Im denotes 1-ethyl-3-methylimidazolium bis (trifluoromethylsulfonyl)imide and TBTP denotes tetrabutylammonium tetraphenyl borate.

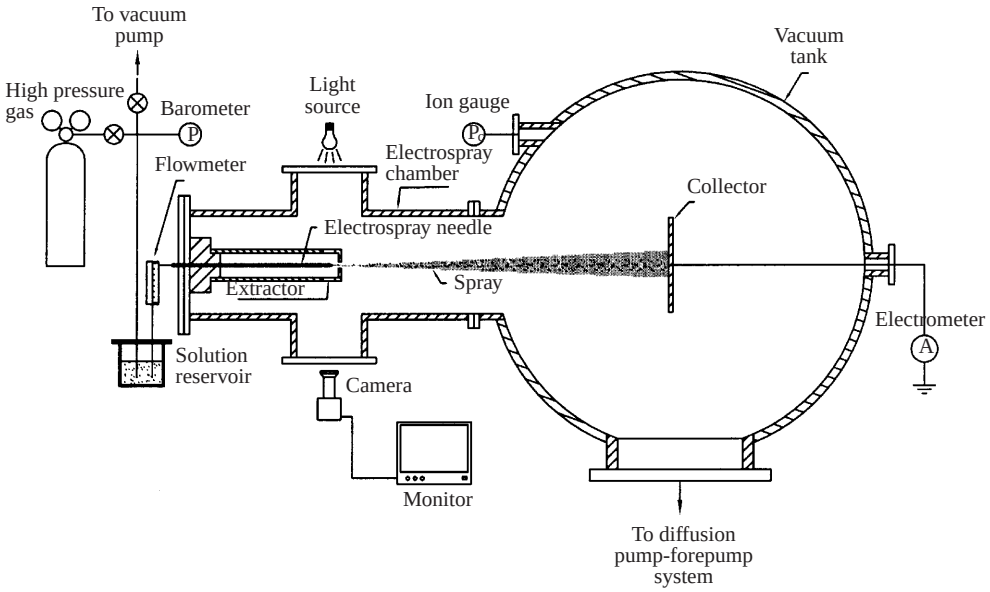

FIGURE 1. Sketch of the electrospray source and vacuum facility.

98% purity) was chosen for its low volatility, a condition required to electrospray liquids in vacuum. A second advantage of TBP is its moderate viscosity: very viscous liquids, such as glycerol, have the tendency to generate electrosprays with a breakup phenomenology that is poorly understood. Table 1 lists the name of each solution, solute concentrations and conductivities. Electrical conductivities are determined by measuring the electrical resistivity across the ends of a capillary tube filled with the liquid solution. The ionic liquid 1-ethyl-3-methylimidazolium bis (trifluoromethylsulfonyl)imide, was used for enhancing the conductivity of TBP1, while tetrabutylammonium tetraphenyl borate was added to the remaining solutions. The surface tension, density, dielectric constant and viscosity coefficient of pure TBP are $\gamma = 0.028\,\mathrm{N\,m^{-1}}$, $\rho = 976\,\mathrm{kg\,m^{-3}}$, $\varepsilon = 8.91$ and $\mu = 0.00359\,\mathrm{Pa\,s^{-1}}$ respectively (Riddick, Bunger & Sakano 1986). We will assume that the modest solute concentrations of the solutions in table 1 do not affect significantly the physical properties of TBP.

Figure 1 shows a schematic of the vacuum facility and electrospray source employed in these experiments. The electrospray source is mounted inside a 5 cm diameter cross (electrospray chamber), joined to a 1×1.3 m cylindrical tank (vacuum tank). The electrodes used to analyse the sprays are installed in this larger chamber. A 25 cm

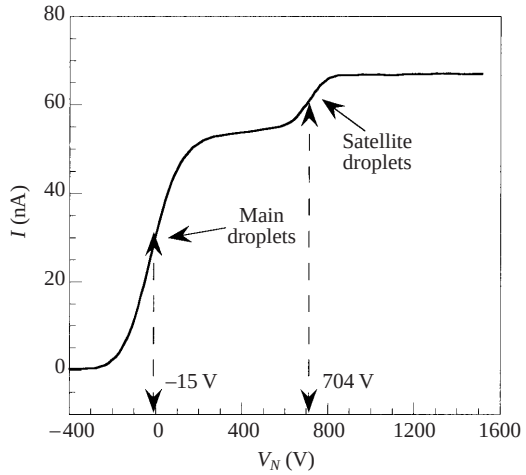

FIGURE 2. Typical stopping-potential curve for an electrospray of solution TBP2.

diffusion pump backed by a mechanical pump evacuates the system down to 10^{-3} Pa. The design of the electrospray source is simple: a plastic reservoir contains the TBP solution, which is fed to the electrospray needle through a fused silica capillary. The liquid flow rate is varied by changing the pressure inside the solution reservoir, and measured by means of a bubble flowmeter connected in series to the fused silica line. The flowmeter is a tube of known diameter, in which a bubble of air can be inserted. The bubble moves with the speed of the flow, and thus the flow rate is equal to the velocity of the bubble multiplied by the area of the tube. The electrospray needle is also a fused silica capillary, with one of its ends connected to the flowmeter while the other is shaped into a cone (needle tip) and made electrically conductive by depositing a layer of tin oxide on its surface. An extractor electrode with a small orifice faces the needle tip. The distance between the tip of the needle and the facing extractor is approximately 2.5 mm. The diameter of the extractor's orifice is roughly 0.8 mm. In order to form a cone-jet, the TBP solution is fed to the needle and an appropriate voltage difference between needle and extractor (typically 1600 V), is set. The shape of the cone-jet is monitored with a microscope connected to a VCR system. In our experiments the needle is charged positively with respect the extractor, and therefore the net charge of the emerging droplets is positive. The beam of droplets exists the needle–extractor region through the extractor orifice, and enters the large vacuum tank where it is subsequently analysed. The experiments were always carried out at room temperature (approximately 24 °C).

A detailed description of the additional arrangement (collector electrodes where the current of the beam is measured, power supplies, electronics, connections, etc.) required for performing stopping-potential and time-of-flight measurements of the electrospray beam was given elsewhere (Gamero-Castaño & Fernández de la Mora 2000; Gamero-Castaño & Hruby 2001). Thus, we will simply outline the experimental techniques here. Figure 2 shows the stopping-potential curve associated with an electrospray of solution TBP2. The flow rate and electric current of this spray are $4.1 \times 10^{-12}\,\mathrm{m^3\,s^{-1}}$ and 66 nA. We plot the electric current measured at a grounded collector facing the beam, approximately 5 cm from the extractor (the collector is located inside the large vacuum tank), as a function of the electrospray needle voltage referred to ground, V_N. The voltage difference between needle and extractor

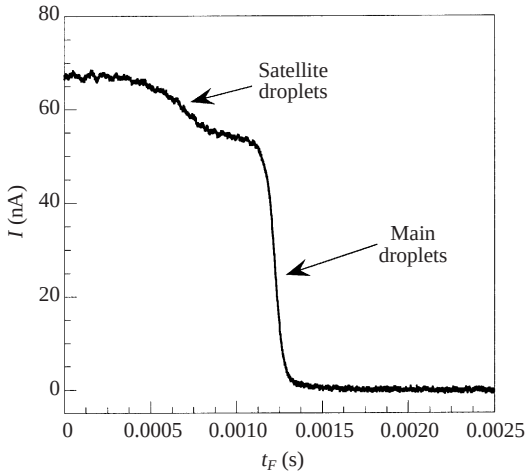

FIGURE 3. Time-of-flight curve for the same spray as in figure 2.

is kept fixed. Therefore both the electrospray inside the needle–extractor region, and the electric current in the form of positively charged droplets exiting the extractor, remain unchanged and independent of V_N. When the potential of the needle is well below ground the positive droplets cannot reach the collector and no current is measured in figure 2. Conversely, for large positive values of V_N the whole current of the electrospray beam is measured at the collector. Main and satellite droplets coexist in this spray: the current associated with the former appears in a range of needle voltage centred around -15 V, while satellite droplets are observed around 704 V. When analysing stopping-potential curves of similar sprays, Gamero-Castaño (1999) erroneously associated the smaller step appearing at larger V_N with the products of in-flight Coulomb fissions of main droplets (see Fernández de la Mora 1996 for a discussion about Coulomb fissions): it seemed unlikely that satellite and main drops, generated at the same point in the jet breakup, could have such disparate stopping voltages. We will show in the paragraphs below why satellite droplets, rather than in-flight Coulomb explosions, are responsible for this smaller step. Continuing with the description of figure 2, we take the value of V_N at one half of the total electric current associated with a given type of droplet as the representative stopping potential, V_S, of that type of droplet. Our definition of V_S, placed at the centre of the error-function-like stopping-voltage distribution, is somewhat arbitrary: there is an important spread of stopping potentials among droplets of the same type, and the values of V_S for either main or satellite droplets could have been placed closer to the beginning or end of each step. A definition with more physical value would require a detailed description of the breakup process, which is unavailable to us at this point. Thus, in figure 2, we take -15 V and 704 V as the 'representative' stopping potentials of main and satellite droplets respectively.

The time-of-flight wave associated with the same TBP2 electrospray is shown in figure 3. After exiting the needle–extractor region, the charged droplets enter the large vacuum tank in figure 1, where the external electric field is null (extractor, vacuum chamber and collector are grounded (earthed); there is still a small electric field associated with the space charge of the beam). Thus, the axial velocity of the droplets remains constant. The whole current of the beam, I, is measured at a collector placed inside the large tank. At a reference time ($t_F = 0$ in figure 3) the electrospraying

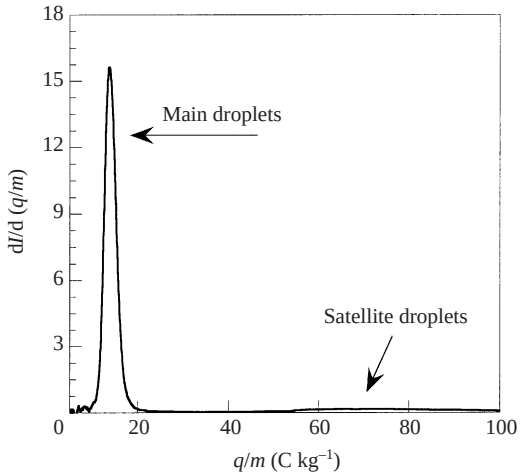

FIGURE 4. Distribution function for the specific charge of the electrospray beam shown in figures 2 and 3.

process is suddenly interrupted, the rear front of the beam moves toward the collector and the current arriving at it is recorded versus time, yielding the time-of-flight wave of figure 3. Note that the same two types of droplets observed previously in the stopping-potential curve appear now in figure 3. The relevant parameter yielded by the time-of-flight curve is the specific charge of the electrospray droplets. Specific charge and time of flight are related by

$$\frac{q}{m} = \frac{1}{2\,(V_N - V_S)} \left(\frac{L}{t_F}\right)^2, \tag{1}$$

where q and m are the charge and mass of the droplet, $V_N - V_S$ and t_F its acceleration voltage and time of flight, and L the length of the flight path. There is a finite spread of the time of flight, and accordingly a spread of the specific charge, for the satellite and main droplets. We will define the specific charge of each type of droplet as the mean of its distribution function. We can construct such distribution by changing in the time of flight wave, $I(t_F)$, the variable t_F for q/m, equation (1), and then taking the derivative, $\mathrm{pdf}(q/m) = \mathrm{d}I/\mathrm{d}(q/m)$. The specific charge distribution for the spray in figures 2 and 3 is shown in figure 4. The mean and the standard deviation of the specific charge of a type of droplet are given by

$$\left\langle \frac{q}{m} \right\rangle = \left[\int_{l_0}^{l_1} x\,\mathrm{pdf}(x)\,\mathrm{d}x\right] \Big/ \left[\int_{l_0}^{l_1} \mathrm{pdf}(x)\,\mathrm{d}x\right], \tag{2}$$

$$\delta\left(\frac{q}{m}\right) = \left\{\left[\int_{l_0}^{l_1} (x - \langle q/m\rangle)^2 \mathrm{pdf}(x)\,\mathrm{d}x\right] \Big/ \left[\int_{l_0}^{l_1} \mathrm{pdf}(x)\,\mathrm{d}x\right]\right\}^{1/2}. \tag{3}$$

For the case of the main droplets, the lower limit of integration is 0, $l_0 = 0$, and the upper limit is a value of the specific charge equidistant from the main and satellite peaks. The mean specific charges of the main and satellite droplets in figure 4 are $14.1\,\mathrm{C\,kg^{-1}}$ and $73.3\,\mathrm{C\,kg^{-1}}$ respectively. In these experiments, the evaporation of liquid from droplets in flight is negligible, and can be ignored when computing the specific charge (Gamero-Castaño & Hruby 2001).

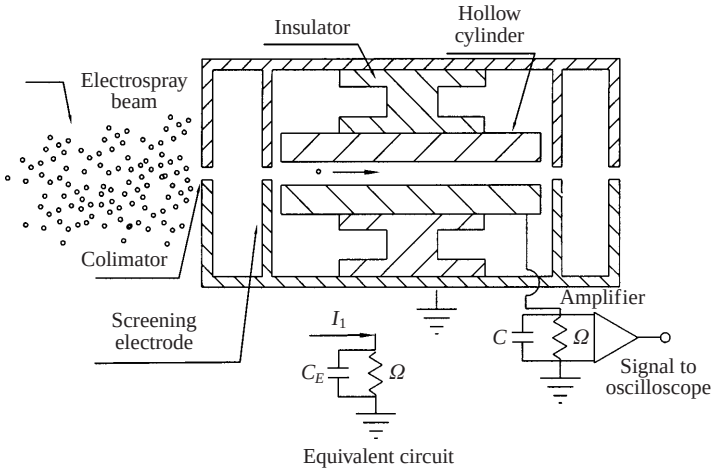

FIGURE 5. Schematic of the capacitive detector used to measure both the charge and specific charge of electrospray droplets.

Now we can ratiocinate why the smaller steps in figures 2 and 3 are associated with satellite drops (produced in the jet breakup), rather than with the products of Coulomb fissions. When a main droplet that is charged above its Rayleigh limit explodes in flight, two types of droplets are produced: a larger fragment containing most of the mass of the original drop and with less specific charge than it, and a few smaller drops with increased specific charge. Thus, if there were Coulomb fissions in these sprays, three distinct steps with the following ordering of specific charges would be recorded in the time-of-flight waves: a step associated with the smaller products of Coulomb explosions, a second one associated with unexploded main droplets, and a third step due to the larger products of Coulomb fissions. But we only observe two different types of droplets in the time-of-flight waves, and therefore the Coulomb fission scenario is not correct.

Both the charge and specific charge of individual droplets can be measured with the capacitive detector shown schematically in figure 5. Hogan & Hendricks (1965) used a similar design, while a more modern and sensitive variation has been used by Fuerstenau & Benner (1995) to measure the mass of viruses. Returning to figure 5, the detector, with its axis roughly aligned with the vertex of the cone-jet, intercepts the electrospray beam. Depending on the aperture of the collimating electrode and the number density of the droplets, a single droplet can be sampled and forced to fly through the hollow metallic cylinder. While this droplet remains inside the cylinder, the potential of the cylinder, V_C, is

$$V_C = \frac{q}{C_C}. \tag{4}$$

where C_C is the capacity between cylinder and ground. This is strictly true in the case of a cylinder isolated from ground. However, the hollow cylinder depicted in figure 5 is connected to ground through a resistor Ω, and the passage of a droplet through its interior translates into two sharp V_C peaks. These peaks are inverted and their tips coincide with the time at which the droplet enters and exits the hollow cylinder. To obtain the evolution of the potential of the hollow cylinder we use the 'equivalent circuit' sketched in figure 5, and simulate the entrance and exit of the charged droplet

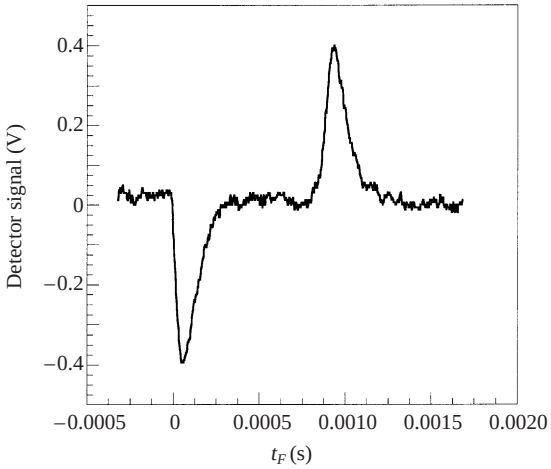

FIGURE 6. Voltage response of the capacitive detector to the passage of a charged droplet through its interior.

by the following impulsive current function:

$$I_1 = \frac{q}{T}[u(t) - u(t-T)] - \frac{q}{T}[u(t-t_F) - u(t-t_F-T)]. \tag{5}$$

Here, $u(t)$ stands for the Heaviside function and t_F is the time of flight of the droplet through the cylinder. T is an arbitrary small time, limited in our system by the 'entrance' time of the droplet $T \sim D_1/v$ (screening electrodes are located at the entrance and exit of the cylinder in order to reduce the characteristic length for the entrance time, D_1). The response of the cylinder voltage to I_1 is given by

$$\begin{aligned} V_C = {} & \frac{q\Omega}{T}[u(t)(1-\exp(-t/\Omega C_E)) - u(t-T)(1-\exp(-(t-T)/\Omega C_E))] \\ & -\frac{q\Omega}{T}[u(t-t_F)(1-\exp(-(t-t_F)/\Omega C_E)) \\ & -u(t-t_F-T)(1-\exp(-(t-t_F-T)/\Omega C_E))] \end{aligned} \tag{6}$$

when the characteristic times of the problem are such that $T < \Omega C_E < t_F$. The evolution of V_C resembles a succession of two inverted peaks of exponential increase. The maximum and minimum of V_C are located at times equal to T and $t_F + T$, respectively. Thus, from the position of the peaks we can deduce the time of flight t_F, and from the droplet's time of flight, the length of the cylinder and acceleration voltage we obtain its specific charge (see equation (1)). We have two options to compute the charge of the droplet. First, if $T \ll \Omega C_E$, q is related to the maximum of the cylinder voltage, V_C^{max}, by

$$q = C_E V_C^{max}. \tag{7}$$

Second, q is also given by the following integral, as can be deduced directly from the differential equation for V_C:

$$q = \frac{1}{2}\int_{-\infty}^{\infty} \frac{|V_C(t)|}{\Omega} \mathrm{d}t. \tag{8}$$

We will use (8) to measure the charge of droplets because the integration of V_C helps filter out the noise associated with the experimental signal. Figure 6 shows a

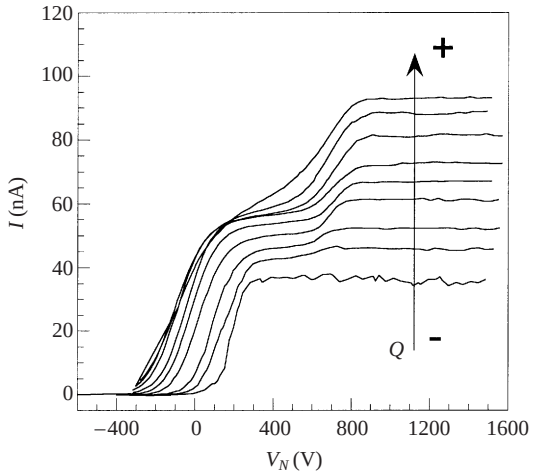

FIGURE 7. Stopping-potential curves of TBP2 electrosprays taken at different flow rates.

typical signal proportional to V_C resulting from the passage of a droplet. We use an inverting amplifier to amplify V_C. The entrance of the droplet into the hollow cylinder at $t \sim 0$ is translated into a sharp raise of V_C (the peak in figure 6 is actually negative because of the inverting amplifier), followed by a relaxation (the hollow cylinder is connected to ground through a resistor). V_C features a second peak of the opposite sign, followed by a relaxation, when the droplet exits the hollow cylinder. In this case, the capacitive detector yields values of 2.81×10^{-14} C and $0.68\,\mathrm{C\,kg^{-1}}$ for the droplet's charge and specific charge. Its diameter,

$$D = \left(\frac{m}{q}\frac{6}{\rho\pi}q\right)^{1/3}, \tag{9}$$

is 4.32 μm.

Before we proceed with the presentation and interpretation of the experimental results, an important distinction between stopping-potential, time-of-flight and capacitive-detector data must be pointed out. The first two techniques yield results representative of the whole electrospray beam (in both cases the complete beam is sampled), while each capacitive-detector measurement corresponds to an individual droplet, sampled at a fixed beam location. In the following section we will use the capacitive detector to estimate mean properties of droplets. We will compute these mean properties (charge, diameter and specific charge) by taking the averages of several samples (typically 30 droplets).

3. Results and discussion

3.1. *Voltage drop and diameter of the jet*

Figures 7 and 8 contain stopping-potential and time-of-flight spectra associated with solution TBP2. Each curve in these figures is associated with a different liquid flow rate Q (the values of some liquid flow rates are collected in table 2). These curves illustrate the phenomenology related to the generation of electrospray droplets. For low flow rates, or alternatively for low electrospray currents ($I \lesssim 30$ nA), only main droplets are formed during the jet breakup. This is inferred from the single step of both stopping-potential and time-of-flight curves. At larger flow rates satellite drops

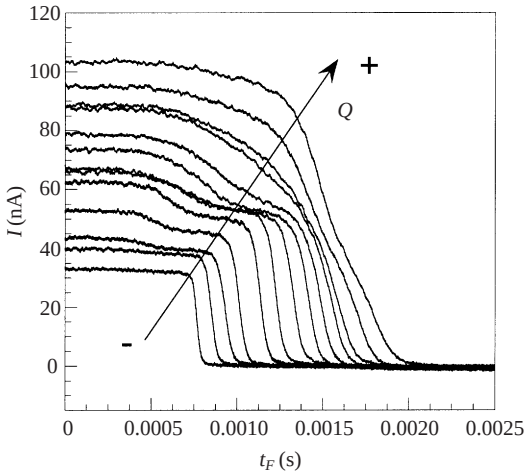

FIGURE 8. Time-of-flight spectra of TBP2 electrosprays.

also emerge from the breakup process. The appearance of satellites is observed in figures 7 and 8 in the form of a second, new, step in the spectra. The fraction of charge emitted as satellite droplets grows with the flow rate, until a new spraying pattern eventually emerges at $I \sim 90\,\mathrm{nA}$. This capillary breakup regime is usually known as kink breakup mode, and is characterized by the onset of large lateral oscillations of the jet (Hartman *et al.* 2000). Gamero-Castaño (1999) has studied in detail the information yielded by the stopping-potential curves associated with the breakup regime in which only main droplets are emitted. He finds that, at low flow rates, a fair fraction of the stopping potential is used in the conversion of conduction current into convected jet surface charge, and thus V_S can be regarded as an irreversible voltage loss. A few lines describing the different regions of the cone-jet are needed to clarify both this statement about the irreversible voltage loss and the forthcoming analysis. The physical models aimed at explaining the mechanism of current transport in cone-jets consider three different regions (Fernández de la Mora & Loscertales 1994; Gañán-Calvo 1997*a*; Cherney 1999): the cone, an intermediate zone at the beginning of the jet, and the rest of the liquid filament. The cone is regarded as nearly electrostatic because of its large cross-section, the electric current being transported by bulk conduction through it. As the cone tip is approached, internal electric fields develop, and charge from the inner liquid is injected on the surface, so that the current is driven simultaneously by bulk conduction and surface charge convection. Eventually, the last term becomes dominant and the total current is convected surface charge. We term this intermediate section a transition region, and the irreversible voltage loss is roughly the voltage drop along it. We qualify this voltage drop as 'irreversible' because it is mostly used to convert conduction current into convected surface charge, rather than to accelerate the fluid. Beyond this point the jet continues to accelerate, forced by the tangential electric field acting on its surface charge. We will show in the following paragraphs that in this portion of the jet extending from the transition region to the breakup location, the electric potential energy is mostly converted into kinetic energy of the fluid. Thus, this section can be properly qualified as reversible. A significant finding of Gamero-Castaño (1999) is the independence of irreversible voltage loss from liquid flow rate, which is compatible

Solution	$Q(\mathrm{m^3\,s^{-1}})$	I(nA)	$\langle q/m\rangle$ main ($\mathrm{C\,kg^{-1}}$)	$\langle q/m\rangle$ sat. ($\mathrm{C\,kg^{-1}}$)	V_S main (V)	V_S sat. (V)	$V_N - V_B$ (V)	V_O (V)	$v_B(\mathrm{m\,s^{-1}})$
TBP1	7.5×10^{-13}	45	59.1	225.9	110	508	649	1469	252
TBP1	9.7×10^{-13}	50	50.2	239.3	85	508	620	1469	232
TBP1	1.16×10^{-12}	54	43.8	228.3	52	493	598	1469	219
TBP2	1.62×10^{-13}	43	26.9	139.4	143	607	718	1547	176
TBP2	2.12×10^{-12}	53	21.7	121.9	75.8	631	751	1547	171
TBP2	3.11×10^{-12}	62	16.7	118.1	21	675	782	1547	159
TBP2	4.10×10^{-12}	66	14.1	73.2	−15	704	876	1547	159
TBP2	5.09×10^{-12}	67	12.0	68.2	−22	702	856	1547	145
TBP3	6.53×10^{-12}	47	7.0	19.1	301	754	1018	1562	100
TBP3	8.62×10^{-12}	53	5.7	17.8	233	825	1103	1609	100
TBP3	1.28×10^{-11}	62	4.2	15.5	198	872	1125	1609	89
TBP3	2.33×10^{-11}	83	2.8	10.0	91	963	1310	1734	83
TBP4	2.06×10^{-11}	45	2.15	6.44	311	810	1060	1766	57
TBP4	2.86×10^{-11}	54	1.77	5.86	273	882	1145	1766	56
TBP4	3.67×10^{-11}	62	1.50	5.80	238	958	1208	1844	54
TBP5	4.00×10^{-11}	41	0.90	2.35	362	891	1221	1624	39
TBP5	5.26×10^{-11}	48	0.78	2.18	361	1019	1385	1703	40
TBP5	7.83×10^{-11}	57	0.64	1.97	348	1105	1468	1766	38
TBP5	9.56×10^{-11}	62	0.57	1.84	290	1232	1657	1766	39

TABLE 2. Voltage drop and velocity at the jet breakup location, and other relevant parameters of the electrospraying process.

with the scaling for the characteristic diameter of the transition region predicted by Gañán-Calvo (1997*a*), $D \sim Q^{1/2}/K^{1/6}$.

In this article we are mostly interested in the intermediate flow rates in which both satellite and main droplets are produced because the voltage difference between the electrospray needle and the jet breakup point, as well as the velocity of the jet at this location, can be inferred when both types of droplets are emitted. To show this, let us recall the expression for the stopping potential of an electrospray droplet (Gamero-Castaño 1999). Upon detachment from the jet, the sum of kinetic and potential energy of the droplet remains constant, $qV + \frac{1}{2}mv^2 = C$. Furthermore, C is exactly zero when the potential field is such that the droplets are stopped at the surface of the collector, since the velocity is null at the surface of the collector and the voltage of this electrode is taken as the reference value. Thus, adding and subtracting the potential of the needle when C is identically zero, and defining the potential of the needle when $C \equiv 0$ as the stopping potential V_S, we obtain

$$V_S = (V_N - V_B) - \frac{1}{2}\frac{m}{q}v_B^2, \tag{10}$$

where the subscript 'B' identifies parameters at the breakup point. The term within brackets is the voltage difference between the base of the Taylor cone and the breakup point, a meaningful characteristic independent of V_N. This independence holds as long as the voltage difference between needle and extractor, V_O, is such that a stable cone-jet is formed. Typically, V_O can be varied within a few hundreds volts without compromising the stability of the cone-jet. At lower V_O a different electrospraying regime called the dripping mode is induced, while a highly stressed mode characterized by the formation of multiple jets is typical of larger V_O (Cloupeau & Prunet-Foch 1990). Note that time-dependent contributions to the electric field in the proximity of the breakup location are neglected in (10). We also will consider that the velocity and electric potential of the fluid remain constant upon its detachment from the jet. This approximation is justified because the difference in either voltage or kinetic energy per unit charge between the emerging droplet and the jet must be of the order of the change during the breakup in surface energy per unit charge, $\gamma Q/(R_B I)$, and we will show in following paragraphs that this group is a small quantity compared to either $\frac{1}{2}(m/q)v_B^2$ or $V_N - V_B$. Furthermore, because main and satellite droplets are generated at the same jet location, we will take the values of $V_N - V_B$ and v_B associated with both types of droplets to be the same.

Once the specific charge and the stopping potential of a droplet have been measured with the time-of-flight and stopping-potential techniques, (10) becomes an algebraic equation with two unknowns, $V_N - V_B$ and v_B. Because two independent equations, one for satellites and another for main droplets, can be set, there is sufficient information to determine both $V_N - V_B$ and v_B. We have determined in this way the voltage drop along the cone-jet and the velocity of the fluid at the breakup location for several electrosprays. Table 2 collects the values of the relevant jet parameters. The electrospray flow rate, measured with the bubble flowmeter, and the electric current are given in the second and third columns. They are followed by the specific charge of main and satellite droplets, and their stopping potentials. The values of $V_N - V_B$ and the voltage difference between needle and extractor, V_O, appear in the eighth and ninth columns. V_O is the available voltage for the electrospraying process. The large fraction of V_O spent in accelerating the jet is noteworthy. For example, $V_O = 1766\,\mathrm{V}$ for the last row of solution TBP5, and as much as 1657 V is used to accelerate the jet. For the most-conducting solution, TBP1, $V_O = 1469\,\mathrm{V}$ and the voltage decrease

in the jet can be as large as 649 V. We will see in the following paragraphs that a fair fraction of this voltage drop is spent reversibly, i.e. the potential decrease is mostly transformed into droplet kinetic energy. In fact, the larger the conductivity, the more correct this statement is. The last column collects the velocity of the fluid at the breakup location.

We can confirm independently the validity of the experimental values of $V_N - V_B$ and v_B given in table 2 using the momentum equation for the jet. The following relation is a good approximation for the momentum balance in the reversible section of the jet, downstream of the transition region:

$$\frac{\mathrm{d}}{\mathrm{d}x}\left(\frac{\rho v^2}{2} + p\right) = E_t \xi, \tag{11a}$$

where E_t is the tangential electric field acting on the surface of the jet, and ξ is the volumetric charge of the jet. Because in this part of the jet ξ remains approximately constant, (11a) can be integrated to obtain the algebraic equation

$$\frac{\rho v^2}{2} + p + \phi\xi = C, \tag{11b}$$

where ϕ is the electric potential and here C a constant of integration. Finally, using $Q = \pi R^2 v$ and $I = \xi Q$, equation (11b) can be rearranged to yield

$$[V_N - V(x)] - \Delta = \frac{1}{2}\frac{Q\rho}{I}v(x)^2 + \frac{Q}{I}\left[\frac{\gamma}{R(x)} - \frac{I^2}{8\varepsilon_0 Q^2}R(x)^2\right]. \tag{11c}$$

In this expression we have split the pressure term into its capillary and electric components. The variable x stands for a generic position along the jet axis, downstream of the transition region; Δ stands for a constant of integration. It is important to gain a better insight into the relative weights of the kinetic, capillary and electric terms in the right-hand side of (11c), and how they vary along the jet axis. For that purpose we utilize the scaling law for the electric current (Fernández de la Mora & Loscertales 1994):

$$\frac{I}{\gamma(\varepsilon_0/\rho)^{1/2}} = f(\varepsilon)\left(\frac{\rho Q K}{\gamma\varepsilon\varepsilon_0}\right)^{1/2} = f(\varepsilon)\eta \tag{12}$$

to eliminate I from (11c), and make the resulting equation dimensionless using the characteristic jet radius r_G^* (Gañán-Calvo 1997a) and irreversible voltage loss V^* (Gamero-Castaño 1999):

$$V^* = \left(\frac{\gamma^2}{K(\rho\varepsilon_0)^{1/2}}\right)^{1/3}, \quad r_G^* = \left(\frac{\rho\varepsilon_0}{\pi^4\gamma K}\right)^{1/6} Q^{1/2}, \quad \chi(x) = \frac{R(x)}{r_G^*} \tag{13a,b,c}$$

$$\frac{V_N - V(x)}{V^*} - \frac{\Delta}{V^*} = \frac{\pi^{2/3}\varepsilon}{2f(\varepsilon)}\eta\frac{1}{\chi(x)^4} + \frac{\pi^{2/3}\varepsilon^{1/2}}{f(\varepsilon)}\frac{1}{\chi(x)} - \frac{f(\varepsilon)}{8\pi^{2/3}}\eta\chi(x)^2. \tag{13d}$$

The terms appearing on the right-hand side of (13d) are the kinetic, capillary and electrostatic pressures respectively; ε is the dielectric constant of the liquid, $\varepsilon = 8.91$ for TBP; $f(\varepsilon)$ is the proportionality constant relating the electrospray current and the dimensionless flow rate η, $f(\varepsilon) = 6.8$ for TBP (Gamero-Castaño 1999). The dimensionless flow rate η is typically of order one. In the reversible part of the jet, the dimensionless radius χ is maximum at its boundary with the transition region, and is a monotonic decreasing function downstream. Figure 9 plots the right-hand side of equation (13d) as a function of χ for $\eta = 1$ and $f(\varepsilon) = 6.8$. Note that this

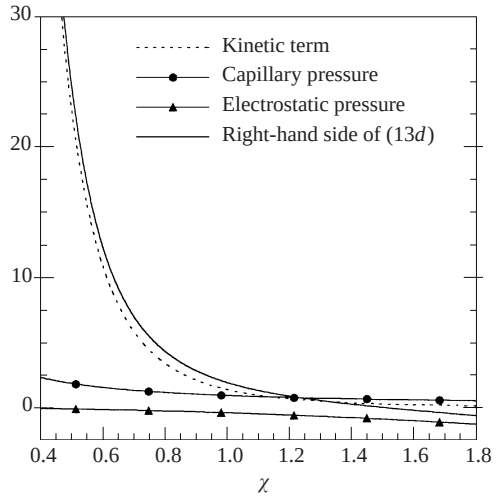

FIGURE 9. Representation of the different terms in equation (13*d*) as a function of the dimensionless radius χ.

function is identically 0 for $\chi = 1.51$. Thus, if the reversible part of the jet started at a radius such that $\chi = 1.51$, the term Δ would coincide with the voltage drop across the transition region. For the case of TBP, the ratio Δ/V^* is approximately constant (Gamero-Castaño 1999). Note also that it is very unlikely that the reversible part of the jet starts at $\chi > 1.33$, since that would indicate that the pressure at the jet would become negative. Although equation (13*d*) itself does not yield information about the value of χ at the breakup location, we can infer the jet radius at this point from the liquid flow rate and our measurement of v_B. The dimensionless jet radii at the breakup point, $\chi(B)$, computed in this way, are given in table 3. Notice that $\chi(B)$ is typically 0.5. It is observed in figure 9 that for $\chi \sim 0.5$, the kinetic energy of the fluid becomes about 92% of the right-hand side of (13*d*). In other words, most of the voltage drop along the reversible part of the jet is spent in accelerating the fluid. It is also clear that the previous statement about $\frac{1}{2}(m/q)v_B^2$ being much larger than $\gamma Q(R_B I)$ is also correct.

Let us now use the data from table 2 to check whether they are consistent with the equation of conservation of momentum for the jet. We will compute the right-hand side of (11*c*) using the measurements of Q, I and the radius of the jet at breakup, and plot this quantity versus $V_N - V_B$. According to (11*c*), a linear relation with unity slope between these points is necessary to validate our measurements of $V_N - V_B$ and v_B. We list in table 3 the voltage drop, and inertial, capillary and electric pressure terms at the jet breakup point associated with the data from table 2. We have used the characteristic voltage V^*, (13*a*), to make these parameters dimensionless. We do not rely on the scaling law (12) to compute the three terms on the right-hand side of (11*c*), but we use the direct measurements of I, Q, and R_B. Figure 10 plots the voltage difference between electrospraying needle and breakup point, versus the addition of the three terms on the right-hand side of (11*c*) (again, we point out that V^* is used to make dimensionless these values). The linearity of the data, in such wide range of electrical conductivities and flow rates, is noteworthy. More interesting is the fact that the slope, 0.95, is close to 1, as expected. Note that the interception with the ordinate axis, with a value of 16.8, is associated with the irreversible voltage drop in the transition region of the cone-jet, Δ/V^*. Δ/V^* was previously found to be

Solution	$Q(\mathrm{m^3\,s^{-1}})$	$R_B(\mu\mathrm{m})$	χ_B	$\frac{V_N - V_B}{V^*}$	Kinetic term	Capillary pressure	Electric pressure
TBP1	7.5×10^{-13}	0.031	0.49	90.4	72.7	2.1	0.1
TBP1	9.7×10^{-13}	0.036	0.51	86.4	70.9	2.0	0.1
TBP1	1.16×10^{-12}	0.041	0.52	83.3	69.8	2.0	0.1
TBP2	1.62×10^{-13}	0.054	0.50	73.0	57.5	1.9	0.1
TBP2	2.12×10^{-12}	0.063	0.51	76.3	58.3	1.8	0.1
TBP2	3.11×10^{-12}	0.079	0.52	79.5	63.0	1.8	0.2
TBP2	4.10×10^{-12}	0.091	0.53	89.0	77.5	1.9	0.2
TBP2	5.09×10^{-12}	0.10	0.55	87.0	79.1	2.0	0.2
TBP3	6.53×10^{-12}	0.14	0.50	59.7	39.8	1.5	0.1
TBP3	8.62×10^{-12}	0.17	0.50	64.7	46.5	1.6	0.1
TBP3	1.28×10^{-11}	0.21	0.53	66.0	46.7	1.5	0.2
TBP3	2.33×10^{-11}	0.30	0.55	76.8	55.5	1.5	0.3
TBP4	2.06×10^{-11}	0.34	0.55	42.8	28.7	1.5	0.1
TBP4	2.86×10^{-11}	0.40	0.56	46.2	32.1	1.4	0.2
TBP4	3.67×10^{-11}	0.46	0.57	48.8	33.7	1.4	0.2
TBP5	4.00×10^{-11}	0.57	0.58	37.2	22.6	1.4	0.1
TBP5	5.26×10^{-11}	0.65	0.57	42.2	26.1	1.4	0.2
TBP5	7.83×10^{-11}	0.81	0.59	44.7	29.3	1.4	0.2
TBP5	9.56×10^{-11}	0.88	0.58	50.5	35.6	1.5	0.2

TABLE 3. Jet breakup parameters required to test (11*c*). Notice that the values in the fifth to eighth columns are made dimensionless using V^*.

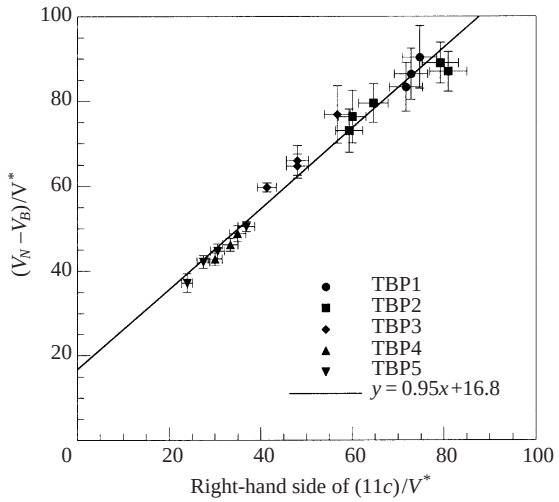

FIGURE 10. Validation of the measurements of $V_N - V_B$ and v_B using the data in table 3 and equation (11*c*).

constant, independent of either the liquid flow rate or electrical conductivity (Gamero-Castaño 1999). The good correlation observed in figure 10 supports the validity of the experimental data in table 2. Furthermore, numerical and analytical models of the cone-jet should yield solutions for these well-defined electro-fluid-dynamic parameters. Hence, their comparison with our experimental data for $V_N - V_B$ and v_B will allow the confirmation or rejection of these electrospray theories.

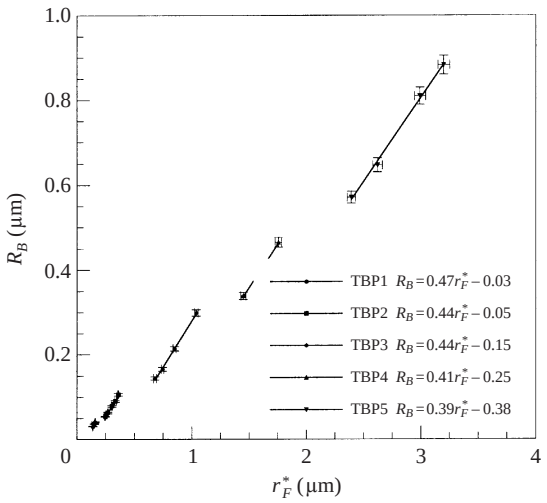

FIGURE 11. Jet diameter at the breakup point versus r_F^*.

The radii of the jets at their breakup points can be used to test the predictions of the two more widely accepted electrospray models. Fernández de la Mora & Loscertales (1994) originally proposed that, for electrosprays of moderate- and high-conductivity solutions such as those studied here, the radius of the jet emerging from a Taylor cone should be equal to the characteristic length r_F^*:

$$r_F^* = \left(\frac{Q\varepsilon\varepsilon_0}{K}\right)^{1/3} \tag{14}$$

multiplied by a function of the dielectric constant of the liquid. The same result is defended by Gañán-Calvo *et al.* (1997) in an independent theoretical analysis. More recently, Gañán-Calvo (1997*a*) maintains that the quantity r_G^*, defined in (13*b*), is the correct scaling length for the jet radius. Before we match these two scaling laws with our data for the radius of the jet, a few comments are necessary. First, for a given liquid the ratio r_F^*/r_G^* depends on small powers of Q and K, which makes difficult a comparison between the two theories. Second, both (13*b*) and (14) are defined as the characteristic radius of the transition region where the conduction current becomes convected surface charge. However, the jet radius at the breakup location is smaller because the fluid is continuously accelerated along the jet. Thus, although R_B could be of the order of r_F^* or r_G^*, R_B does not have to be, in principle, strictly proportional to either length. Despite this, Chen & Pui (1997), Gañán-Calvo *et al.* (1997) and de Juan & Fernández de la Mora (1997) have found that the radii of electrospray droplets fit well the relation $R_D = G(\varepsilon)r_F^*$, and thus these experimental findings support Fernández de la Mora & Loscertales's (1994) scaling law. Rosell-Llompart & Fernández de la Mora (1994) also found that the radii of electrospray droplets scales very approximately with r_F^*, but they noticed a scattering of the values of $G(\varepsilon)$ which is attributed to the effect of inertia and viscosity on the jet dynamics. That inertia must be indeed important for the determination of R_B is apparent from the relative weight of the kinetic, capillary, and electric terms in table 3. On the other hand, though in the work of Gañán-Calvo (1997*a*) the dynamic of the jet is analysed, the breakup is not considered either. Although Gañán-Calvo cannot predict precisely where the jet ends, he is still able to ratiocinate an expression for R_B, namely $R_B \approx 0.6r_G^*$.

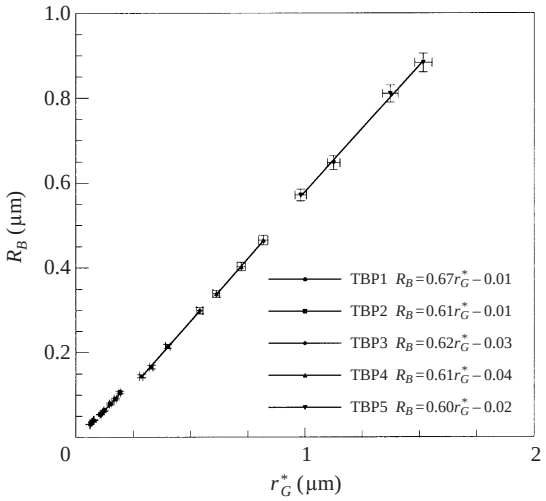

FIGURE 12. Jet diameter at the breakup point versus r_G^*.

Figure 11 plots R_B versus r_F^*. Note that for each TBP solution, a straight line fits well the R_B, r_F^* data. Each fitting has a non-negligible interception with the ordinate axis, and their slopes increase with the conductivity of the solution. The resulting scatter in the value of $G(8.91)$ (we find an average value of 0.25 for G, with a standard deviation of the data relative to their average of 9.3%) could be due to the effects of inertia and viscosity as shown by Rosell-Llompart & Fernández de la Mora (1994). The theory of Gañán-Calvo (1997*a*) is tested in figure 12. R_B scales well with r_G^*, especially for the four less-conducting solutions. The interceptions of the fitting are always small, and their slopes practically coincide and are very similar to the value of 0.6 predicted by Gañán-Calvo (1997*a*).

3.2. *Varicose breakup of viscous, charged jets*

Stability analyses of capillary jets yield good agreement between experimental and model results. When the shape of a capillary cylinder in equilibrium is distorted by a small sinusoidal perturbation, the disruption may grow, or die out, depending on the ratio between the perturbation wavelength and cylinder diameter. Several authors have investigated the effect of electrification on the breakup of capillary jets. Saville studies the cases of a charged jet in the absence of an external electric field (Saville 1971*a*) and an uncharged jet in a uniform tangential field (Saville 1971*b*). The problem of a charged jet immersed in a tangential electric field is analysed by Mestel in the limits of high (Mestel 1994) and low Reynolds number (Mestel 1996). The interpretation of the breakup of cone-jets based on these theoretical results is difficult, for not much is known about the actual conditions under which electrospray droplets are formed. The recent work of López-Herrera *et al.* (1999) is more oriented to actual cone-jets, and considers relevant issues such as the determination of the most unstable wavelength, the generation of satellites or the distribution of mass and charge between main and satellite droplets. When these authors model the effect of electricity on the jet breakup, they consider the liquid to be a perfect conductor. Accordingly, the jet boundary becomes an equipotential surface in their model. However, this hypothesis, as valid as any other from a mathematical point of view, might not be fulfilled in cone-jets of dielectric liquids. The experimental evidence offered by de Juan & Fernández de la Mora (1997) indicates that the specific charge distribution

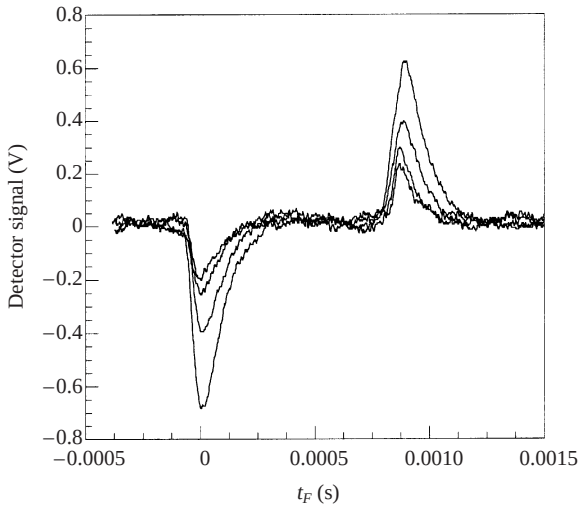

FIGURE 13. Capacitive detector waves for several droplets of the same electrospray.

of the main droplets is narrower than their radius distribution. This observation is incompatible with the equipotential hypothesis, which predicts that the distribution in specific charge is approximately two times wider than the distribution in radius. If the liquid were a perfect conductor, the main droplet's specific charge would be inversely proportional to the square of its diameter. In this case the relative deviations (we use this figure to characterize the width of a distribution) of the specific charge and radius distributions and related by

$$\frac{\delta(q/m)}{\langle q/m\rangle} = 2\frac{\delta(R)}{\langle R\rangle} + O\left[\left(\frac{\delta(R)}{\langle R\rangle}\right)^2\right]. \tag{15}$$

The measurements taken with the capacitive detector support de Juan & Fernández de la Mora's findings with increased resolution. Figure 13 collects several capacitive detector spectra associated with droplets of an electrospray of solution TBP5, at fixed flow rate $Q = 7.83 \times 10^{-11}$ m^3 s^{-1}. Each curve is the trace associated with a single drop of the same electrospray, and only droplets travelling in a small and fixed location within the beam are sampled. Note that, despite the fact that the times of flight of the droplets are basically the same (the time of flight being the difference in time between the tips of the peaks), the areas of the peaks are quite different (the areas of the peak being proportional to the net charge of the droplet). Hence, the specific charges of different droplets appear to be constant, while their charges and diameters vary noticeably. Specifically, the relative deviations of the specific charges and diameters of 30 droplet samples of the spray in figure 13 are 3.6% and 11% respectively.

Our time-of-flight curves are also in contradiction with the equipotential hypothesis. Using the methodology outlined in § 2, we have computed the relative deviation of the specific charge distributions of every time-of-flight wave recorded. These data are compiled in figure 14. Flow rates below and above the onset of satellite droplet formation appear in figure 14. Notice that the relative deviations are remarkably low, typically 8%. The relative deviation for the lowest flow rate of TBP2 is as small as 5.5%. In fact, it can be argued that the data plotted in figure 14 are overestimates of the relative deviations of the electrosprays: because the entire beam is being measured at the time-of-flight collector without the help of focusing lenses, droplets

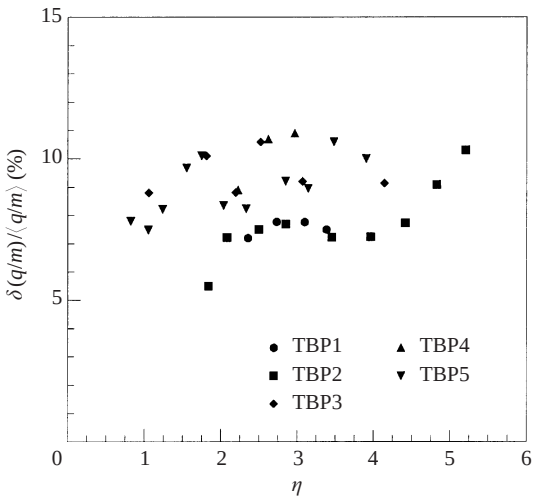

FIGURE 14. Relative deviation of the specific charge of main droplets versus dimensionless flow rate η.

travelling on the outer part of the spray intercept the collector with a considerable radial velocity. Although this radial velocity is mostly induced by the space charge of the spray, one can imagine that a fraction of the axial kinetic energy of the droplets is also converted into radial kinetic energy. Comparable data dealing with the radius distribution function of similar sprays can be found in the literature. The relative deviations of the radius distributions measured by de Juan & Fernández de la Mora (1997) are between 8.5% and 13%. The three narrowest radius distributions given in figure 3(*a*) of Rosell-Llompart & Fernández de la Mora (1994) have relative deviations of 8.5%, 12% and 13%. Relative deviations between 9.0% and 12.2% are obtained from figures 5(*a*) and 6 of Chen, Pui & Kaufman (1995). Thus, the radius distributions are wider than the specific charge distributions.

We conclude that the breakup of cone-jets of dielectric liquids does not occur at constant electric potential. Nevertheless, reliable calculations of the breakup require a simplified and satisfactory model for the distribution of charge in the jet. After observing the narrowness of the time-of-flight spectra, one is tempted to consider the limiting and simple case of jet breakup at constant volumetric charge. However this hypothesis is not appropriate either, since it does not account for the noticeable difference in specific charge between main and satellite droplets. We propose that among the scenarios that can be easily implemented in calculations of jet breakup, that of charge bounded to the surface resembles best the phenomena occurring in real cone-jets. In this hypothesis the net charge remains on the surface of the jet, no transfer of charge is allowed between the liquid bulk and its surface, the electric field inside the jet is negligible, and convection of surface charge dominates over bulk and surface conduction. We will show that this hypothesis is consistent with the observed narrowness of the specific charge distribution for the main drops, while allowing for a different distribution of specific charge between main and satellite droplets.

In the following paragraphs we extend Chandrasekhar's analysis to include the effect of surface charge on the capillary breakup of viscous jets (Chandrasekhar 1981). Three limiting cases will be solved: charge bounded to the jet surface, constant

volumetric charge, and equipotential jet. We aim to investigate the differences and similarities resulting from these three hypotheses.

Let us consider a uniform infinite cylinder of an incompressible, viscous, electrically charged fluid, and disturb its shape so the deformed surface is described by

$$R_j = R_0(1 + \varepsilon e^{\sigma t + ikz}), \tag{16}$$

where R_0 is the radius of the undisturbed jet, and σ, k and εR_0 the growth rate, the wavenumber and the amplitude of the axial disturbance respectively. The motion of the fluid will be studied using a cylindrical coordinate system moving in the axial direction at a constant speed equal to the velocity of the undisturbed jet. The goal of the stability analysis is to find the values of k for which the disturbance grows in time for any arbitrary small value of ε, i.e. the values of k for which σ is positive. Furthermore the analysis will yield the critical wavenumber k^* that maximizes the growth rate, and from k^* we will obtain the critical wavelength λ^* at which the jet is most probable to break into droplets ($\lambda^* = 2\pi/k^*$). Let us write the velocity vector $\boldsymbol{u}$, pressure p and surface charge α as power series of the small parameter ε:

$$\boldsymbol{u} = \varepsilon \boldsymbol{u}_1(r) e^{\sigma t + ikz} + O(\varepsilon^2), \tag{17}$$

$$p = p_0 + \varepsilon p_1(r) e^{\sigma t + ikz} + O(\varepsilon^2), \tag{18}$$

$$\alpha = \alpha_0 + \varepsilon \alpha_1 e^{\sigma t + ikz} + O(\varepsilon^2). \tag{19}$$

The momentum and mass conservation equations for the first-order terms are

$$\frac{\partial \boldsymbol{u}_1}{\partial t} = -\nabla \frac{p_1}{\rho} + \nu \nabla^2 \boldsymbol{u}_1, \tag{20}$$

$$\nabla \cdot \boldsymbol{u}_1 = 0, \tag{21}$$

when ν is the kinematic viscosity. The acceleration induced by a tangential electric field acting upon either a volumetric or surface net charge distribution will not be considered. The general solutions for the pressure and the radial and axial components of the velocity consistent with the deformed surface (16) are (Chandrasekhar 1981)

$$u_{1r} = k \left[A \mathrm{I}_1(sr) - \frac{R_0 \Pi}{\sigma} \mathrm{I}_1(kr) \right], \tag{22}$$

$$u_{1z} = \mathrm{i} \left[As \mathrm{I}_0(sr) - \frac{R_0 \Pi}{\sigma} k \mathrm{I}_0(kr) \right], \tag{23}$$

$$p_1 = \rho R_0 \Pi \, \mathrm{I}_0(kr), \tag{24}$$

where A and Π are constants of integration, and I_n stands for the Bessel function of purely imaginary argument of order n that is regular at the origin. The scalar s is defined by

$$s^2 = k^2 + \sigma/\nu. \tag{25}$$

The set of differential equations (20) and (21) is complemented by the kinematic boundary condition for the radial component of the velocity at the cylinder's surface

$$\begin{aligned} u_r &= \varepsilon k \left[A \mathrm{I}_1(sR_0) - \frac{R_0 \Pi}{\sigma} \mathrm{I}_1(kR_0) \right] e^{\sigma t + ikz} \\ &= \frac{\partial R_j}{\partial t} + u_z \frac{\partial R_j}{\partial z} = \varepsilon R_0 \sigma e^{\sigma t + ikz} + O(\varepsilon^2) \end{aligned} \tag{26}$$

and two additional boundary conditions for the stresses on the cylinder's surface:

$$\tau_{rz} = v\rho\left(\frac{\partial u_r}{\partial z} + \frac{\partial u_z}{\partial r}\right) = 0 \quad \text{at} \quad r = R_j, \tag{27a}$$

$$\tau_{rr} = p + \tfrac{1}{2}\varepsilon_0 E_n^2 - 2v\rho\frac{\partial u_r}{\partial r} = \gamma\left(\frac{1}{R_1} + \frac{1}{R_2}\right) \quad \text{at} \quad r = R_j, \tag{27b}$$

where R_1 and R_2 are the principal radii of curvature of the deformed cylinder, and E_n the component of the electric field normal to the jet surface. Upon inserting the expressions for u_r and u_z, equation (27a) becomes

$$\varepsilon\left[A\mathrm{I}_1(sR_0)(k^2 + s^2) - 2\frac{R_0k^2\Pi}{\sigma}\mathrm{I}_1(kR_0)\right]\mathrm{i}\mathrm{e}^{\sigma t + \mathrm{i}kz} + O(\varepsilon^2) = 0. \tag{28a}$$

On the other hand, if we linearize the curvature term and use (19) to write E_n in terms of the surface charge, equation (28a) is rewritten as

$$\varepsilon\left\{\rho R_0\Pi\ \mathrm{I}_0(kR_0) + \frac{\alpha_0\alpha_1}{\varepsilon_0} - 2v\rho k\left[As\mathrm{I}_1'(sR_0) - \frac{kR_0\Pi}{\sigma}\mathrm{I}_1'(kR_0)\right] + [1 - (kR_0)^2]\frac{\gamma}{R_0}\right\}\mathrm{e}^{\sigma t + \mathrm{i}kz} + \left(p_0 + \frac{1}{2\varepsilon_0}\alpha_0^2 - \frac{\gamma}{R_0}\right) + O(\varepsilon^2) = 0. \tag{28b}$$

Expression (25) and the terms of first order in equations (26), (28a) and (28b) can be used to construct a system of four algebraic equations and six unknowns, A, Π, s, α_1, σ and k. Thus, once we determine the first-order term of the surface charge, the required relation between growth rate and wavenumber $\sigma(k)$ can be obtained. In the following paragraphs we will use the three hypotheses for the surface charge in order to compute α_1.

Case 1. Charge bounded to the jet surface

If we assume that the electric field in the interior of the jet is negligible and convection current dominates over conduction current on the jet surface, the following continuity equation is obtained from charge conservation:

$$\frac{\mathrm{d}}{\mathrm{d}t}\int\!\!\int_S \alpha \mathrm{d}S = 0 \tag{29a}$$

where $\mathrm{d}/\mathrm{d}t$ is the material derivative on the two-dimensional space defined by the jet surface. Upon manipulation of (29a) surface charge and velocity are related by (Aris 1989)

$$\frac{\partial\alpha}{\partial t} + \nabla_s \cdot (\boldsymbol{V}_s\alpha) + \frac{\alpha}{2a}\frac{\partial a}{\partial t} = 0 \tag{29b}$$

where ∇_s stands for the surface divergence, $\boldsymbol{V}_s$ is the velocity of the fluid on the surface and a is the determinant of the metric tensor for the two-dimensional space,

$$a = \left[1 + \left(\frac{\partial R_j}{\partial z}\right)^2\right]R_j^2. \tag{30}$$

Equating the terms of the same order in (29b) the following expression is obtained for the surface charge:

$$\alpha = \alpha_0 - \varepsilon\alpha_0\left[1 + \frac{k}{\sigma}\mathrm{i}u_{1,z}(R_j)\right]\mathrm{e}^{\sigma t + \mathrm{i}kz} + O(\varepsilon^2). \tag{31}$$

We now use this result to eliminate A and Π from (26), (28a) and (28b) and write

$$\sigma\frac{R_0^2}{v} = y^2 - x^2, \tag{32}$$

$$2x^2(x^2+y^2)\frac{\mathrm{I}_1'(x)}{\mathrm{I}_0(x)}\left[1-\frac{2xy}{(x^2+y^2)}\frac{\mathrm{I}_1(x)\mathrm{I}_1'(y)}{\mathrm{I}_1'(x)\mathrm{I}_1(y)}\right]-(x^4-y^4)$$
$$= J\left\{x(1-x^2)\frac{\mathrm{I}_1(x)}{\mathrm{I}_0(x)} - \Psi\frac{x^4}{x^2-y^2}\left\{1+\frac{y^2}{x^2}+\frac{\mathrm{I}_1(x)}{x\mathrm{I}_0(x)}\left[1-\frac{y^2}{x^2}-2y\frac{\mathrm{I}_0(y)}{\mathrm{I}_1(y)}\right]\right\}\right\}, \tag{33}$$

$$y = sR_0, \quad x = kR_0. \tag{34a,b}$$

These algebraic equations can be solved to obtain the desired relation $\sigma(k, J, \Psi)$, where the viscosity, J, and charge, Ψ, parameters are defined by

$$J = \frac{\gamma R_0}{\rho v^2}, \tag{35}$$

$$\Psi = \frac{\alpha_0^2 R_0}{\gamma\varepsilon_0}. \tag{36a}$$

The viscosity parameters for the cone-jets studied in this article are of order one or smaller, reaching a value as low as 0.06 for the lowest flow rates of TBP1. Thus, the breakup of these jets is strongly viscous. On the other hand, it is worth mentioning that the charge parameter is conveniently written in terms of the current and the volumetric flow rate emitted by the cone-jet as

$$\Psi = \frac{I^2 R_0^3}{4Q^2\gamma\varepsilon_0}. \tag{36b}$$

Notice that the equilibrium between normal stresses on the surface of the undisturbed jet constrains the charge parameter to be smaller than 2. We will show that our jets are charged well below the 'Rayleigh' limit of $\Psi = 2$. Indeed, typical values for the charge parameter of these cone-jets are of the order of 0.25, i.e. approximately 12% of the Rayleigh limit. Despite this, most droplets of the electrospray are charged to a larger fraction of their Rayleigh limit (de Juan & Fernández de la Mora 1997 record some electrospray droplets with a net charge at the Rayleigh limit). Using (36a) to define a charge parameter for a drop, Ψ_d, based on its radius R_d and surface charge, the droplet will reach its Rayleigh limit when $\Psi_d = 4$. Because the specific charge of the fluid remains almost constant upon jet breakup, the charge parameters of the droplet and the jet are related by $\Psi_d/\Psi = (2/3)(R_d/R_0)^2$. When the mean droplet radius is considered, $\langle R_d\rangle/R_0$ is always larger than 1.89, a ratio associated with the inviscid limit. For the viscous jets considered here, $\langle R_d\rangle/R_0$ is in the neighbourhood of 2.6, and for the larger droplets of the distribution R_d/R_0 is even larger. This explains why the electrospray droplets can be close to the Rayleigh limit while the jet is much less charged.

Case 2. Constant volumetric charge ξ_0

When this hypothesis is considered the expression for the surface charge is readily obtained from geometric considerations alone:

$$\alpha = \tfrac{1}{2}\xi_0 R_j, \tag{37}$$

$$\alpha_0 = \alpha_1 = \tfrac{1}{2}\xi_0 R_0 \tag{38}$$

After some manipulation, our system of algebraic is reduced to the following, more compact, set of relations: equation (32)

$$\sigma \frac{R_0^2}{v} = y^2 - x^2,$$

and

$$2x^2(x^2+y^2)\frac{\mathrm{I}_1'(x)}{\mathrm{I}_0(x)}\left[1 - \frac{2xy}{(x^2+y^2)}\frac{\mathrm{I}_1(x)\mathrm{I}_1'(y)}{\mathrm{I}_1'(x)\mathrm{I}_1(y)}\right] - (x^4 - y^4) = J\left[x(1-x^2)\frac{\mathrm{I}_1(x)}{\mathrm{I}_0(x)} + \Psi x\frac{\mathrm{I}_1(x)}{\mathrm{I}_0(x)}\right]. \quad (39)$$

Case 3. Equipotential breakup

We write the electric potential as a power series:

$$\phi = \phi_0(r) + \varepsilon\phi_1(r)\mathrm{e}^{\sigma t + \mathrm{i}kz} + O(\varepsilon^2), \quad (40)$$

where the function ϕ is a solution of Laplace's equation that must remain constant on the disturbed jet surface (we can always set this constant to be zero $\phi(R_j) = 0$). The first term on the right-hand side of (40) is

$$\phi_0(r) = c_1 \ln(r/R_0). \quad (41)$$

The integration constant c_1 is given by the value of the electric field on the undisturbed jet surface

$$E_n(R_0) = -\frac{\mathrm{d}\phi_0}{\mathrm{d}r}\bigg|_{R_0} = -\frac{c_1}{R_0} = \frac{\alpha_0}{\varepsilon_0}. \quad (42)$$

On the other hand, $\phi_1(r)$ is the solution of the Bessel equation

$$\frac{\mathrm{d}^2\phi_1}{\mathrm{d}(kr)^2} + \frac{1}{kr}\frac{\mathrm{d}\phi_1}{\mathrm{d}(kr)} - \phi_1 = 0, \quad (43a)$$

$$\phi_1 = c_2\mathrm{I}_0(kr) + c_3\mathrm{K}_0(kr), \quad (43b)$$

where c_2 is zero because the electrical potential is regular outside the jet, and c_3 is found by imposing ϕ to be zero in the deformed jet surface. To first order, c_3 is given by

$$c_3 = \frac{\alpha_0}{\mathrm{K}_0(kR_0)\varepsilon_0}. \quad (44)$$

Once the functional form of the electrical potential is known, (42) is used again to find the expression for the surface charge in the equipotential breakup:

$$\alpha = \varepsilon_0 E(R_j) = -\varepsilon_0\frac{\mathrm{d}\phi}{\mathrm{d}r}\bigg|_{R_j} = \alpha_0 - \varepsilon\alpha_0\left[1 + \frac{x\mathrm{K}_0'(kR_0)}{\mathrm{K}_0(kR_0)}\right]\mathrm{e}^{\sigma t + \mathrm{i}kz} + O(\varepsilon^2), \quad (45)$$

and with this information the implicit relation for $\sigma(kR_0)$ is written as equation (32)

$$\sigma \frac{R_0^2}{v} = y^2 - x^2,$$

and

$$2x^2(x^2+y^2)\frac{\mathrm{I}_1'(x)}{\mathrm{I}_0(x)}\left[1 - \frac{2xy}{(x^2+y^2)}\frac{\mathrm{I}_1(x)\mathrm{I}_1'(y)}{\mathrm{I}_1'(x)\mathrm{I}_1(y)}\right] - (x^4 - y^4) = J\left\{x(1-x^2)\frac{\mathrm{I}_1(x)}{\mathrm{I}_0(x)} - \Psi\frac{x\mathrm{I}_1(x)}{\mathrm{I}_0(x)}\left[1 + \frac{x\mathrm{K}_0'(x)}{\mathrm{K}_0(x)}\right]\right\}. \quad (46)$$

In figure 15 we plot the dispersion relation for the three breakup hypotheses considered above. The $\sigma(kR_0)$ curves are computed for fixed values of the viscosity and charge parameters, J and Ψ. Notice that the growth rates associated with the cases of constant volumetric charge and charge bounded to the surface are similar, and quite different from the results for equipotential breakup. For constant volumetric charge and charge bounded to the surface, the presence of charge always speeds up the jet breakup in the range of J of figure 15. In an equipotential jet, surface charge slows down the growth rate of small wavenumbers, and speeds up the breakup associated with larger k. For the three cases of electrification, wavelengths shorter than $2\pi R_0$ are unstable, which is not possible for uncharged jets.

The modelling of the surface charge also affects the abscissa position of the maxima of the dispersion relation. This is shown in figure 16, where we plot the critical droplet radius for capillary breakup as a function of the viscosity and charge parameters, for the three electrification cases. Critical wavelength and droplet radius are related by

$$\frac{R_d^*}{R_0} = \left(\frac{3}{4}\frac{\lambda^*}{R_0}\right)^{1/3}. \tag{47}$$

The critical radius of the droplets produced in the breakup of electrified jets is slightly smaller than their uncharged counterparts; the larger the charge parameter the smaller the critical droplet radius. In the case of uncharged jets (47) asymptotes to 1.89 for large J and increases steeply for $J \lesssim 1$. In fact, for very viscous jets the dispersion relation does not have a maximum but the growth rate increases monotonically for decreasing wavenumbers (Chandrasekhar 1981). We observe in figure 16 that charged jets exhibit a similar trend. The differences in the curves $\langle R_d \rangle / R_0$ versus J for different electrification hypotheses are generally small. However, for $J \lesssim 1$ and $\Psi \gtrsim 0.3$ the curve associated with the equipotential breakup clearly separates from the line for uncharged breakup, yielding droplets much smaller than those predicted by either the uncharged, constant volumetric charge or charge bounded to surface solutions. Mean droplet radii measured for several electrosprays with the capacitive detector are also shown in figure 16. For reference, measurements of droplet mean radius, charge and specific charge, along with $\langle R_d \rangle / R_B$ and viscosity and charge parameters are collected in table 4. We have used the values of the jet radius at the breakup point, R_B, instead of the 'undisturbed' jet's radius, R_0, to compute J and Ψ. Note that the charge parameter is relatively small in all cases, well below the Rayleigh limit of $\Psi = 2$. On the other hand viscosity plays a considerable role in the breakup of cone-jets of moderately and highly conductive liquids, as indicated by the low values of J in table 4 (for the lowest flow rate of TBP1 in table 2 the viscosity parameter is 0.06). Returning to figure 16, it is observed that our experimental data for the droplet mean radius fall above the theoretical predictions, the difference being $\sim 15\%$ typically. This moderate disagreement could be due to several reasons. The inclusion of second-order effects in the breakup model might be necessary for attaining a more precise description. The effect of the axial electric field, induced by external electrodes and the charge on the jet, was not considered in any of the electrification cases we have studied. Most likely, the main factor causing the disagreement is our underestimate of the jet radius, $R_0 = (Q/\pi v_B)^{1/2} = R_B$, computed with the velocity of the jet at the jet breakup location. Notice that at this point the surface disturbances are fully developed, and it is apparent that the velocity used to estimate R_0 should be taken somewhere upstream of the breakup location, where the disturbance begins to grow. Hence, the appropriate value for R_0 should be larger than R_B. From the

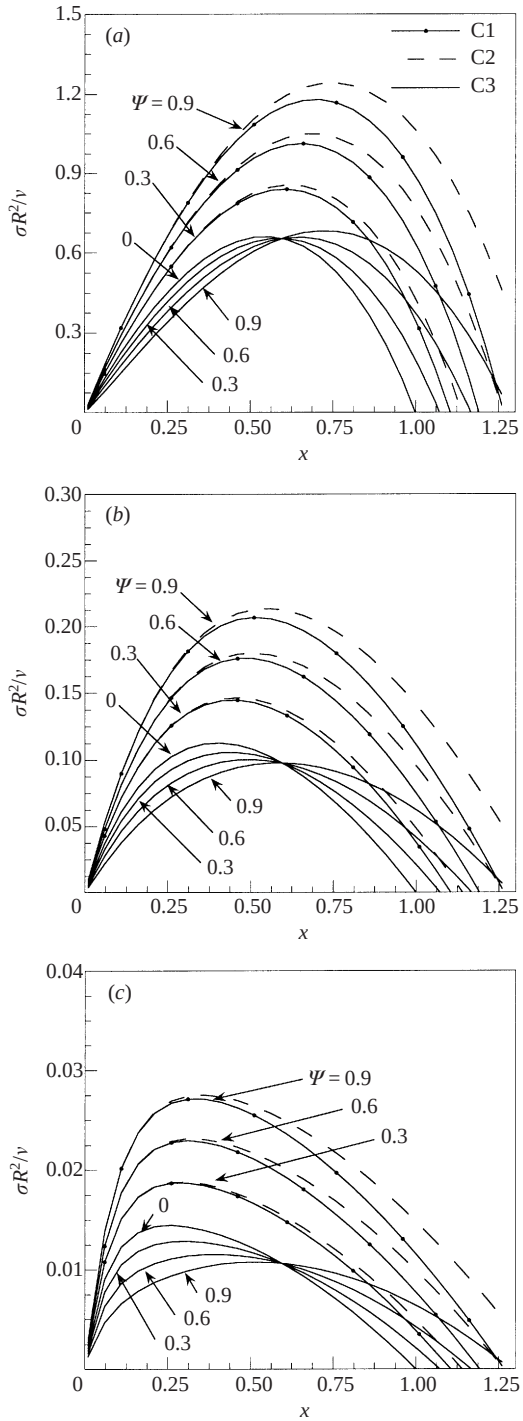

FIGURE 15. Dispersion relation for capillary breakup. We plot the growth rate in units of ν/R_0^2 (y-axis) versus the wavenumber in units of $1/R_0$ (x-axis). In each graph we draw the dispersion relations for the three breakup hypotheses, i.e. charge bounded to jet's surface (C1), constant volumetric charge (C2), and equipotential breakup (C3). The viscosity parameter J is (a) 10, (b) 1, and (c) 0.1, while different charge parameters Ψ are associated with each curve.

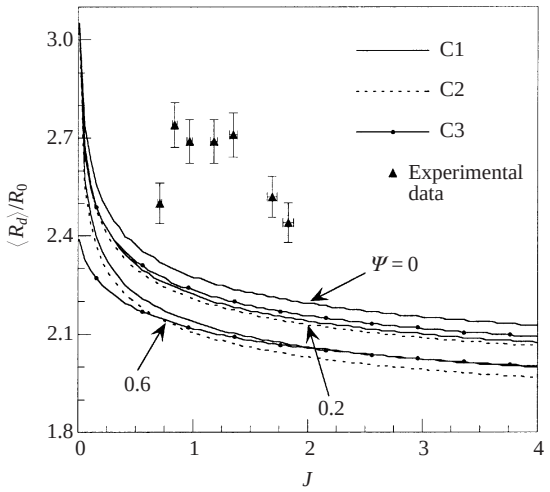

FIGURE 16. Droplet mean radius as a function of the viscosity parameter J. The droplet radius is given in units of the jet radius, R_0. The three breakup hypotheses are shown, as well as different values of the charge parameter Ψ. We also plot experimental values of $\langle R_d \rangle / R_0$.

Solution	$Q(\mathrm{m^3\,s^{-1}})$	$\langle R_d \rangle(\mu\mathrm{m})$	$\langle q \rangle(\mathrm{C})$	$\langle q/m \rangle(\mathrm{C\,kg^{-1}})$	$\langle R_d \rangle / R_B$	J	Ψ
TBP4	2.06×10^{-11}	0.85	5.96×10^{-15}	2.36	2.50	0.71	0.20
TBP4	2.86×10^{-11}	1.11	1.01×10^{-14}	1.78	2.74	0.84	0.25
TBP4	3.67×10^{-11}	1.25	1.34×10^{-14}	1.66	2.69	0.97	0.30
TBP5	4.00×10^{-11}	1.53	1.50×10^{-14}	1.01	2.69	1.18	0.20
TBP5	5.26×10^{-11}	1.75	1.96×10^{-14}	0.87	2.71	1.35	0.23
TBP5	7.83×10^{-11}	2.05	2.59×10^{-14}	0.71	2.52	1.69	0.30
TBP5	9.56×10^{-11}	2.14	2.83×10^{-14}	0.69	2.44	1.83	0.30

TABLE 4. Mean values of the radius, charge and specific charge of electrospray droplets obtained with the capacitive detector, and jet viscosity and charge parameters.

discussion in § 3.1 we know that the radius of the jet varies along the reversible region from approximately $1.35r_G^*$, close to cone tip, to approximately $0.5r_G^*$ at the breakup. An intermediate value of $R_0 \approx 0.57r_G^*$ would be sufficient to collapse the experimental and model results in figure 16. Finally, the data in this figure cannot be used to discriminate among the three different charging hypotheses because the differences between the models are smaller than the difference between the experimental data and the theoretical predictions.

We are now in a position to obtain an alternative scaling law for the mean diameter of the main electrospray droplets. Because the volumetric charge in the reversible part of the jet is approximately constant, and the kinetic term $\rho v^2/2$ of the fluid at the breakup location is much larger than its pressure, the velocity of the jet can be approximated by

$$v_B = \left(\frac{2I}{\rho Q} V_A \right)^{1/2} \tag{48}$$

where V_A is the acceleration voltage of the jet. The radius of the jet is simply $R_B = (Q/\pi v_B)^{1/2}$, and we use R_B and the functions plotted in figure 16 to obtain the

droplet mean radius

$$\langle R_d \rangle = h(J, \Psi) R_B = h(J, \Psi) \left(\frac{\rho Q^3}{2\pi^2 I V_A} \right)^{1/4}. \tag{49a}$$

Knowledge of Q, I, V_A and the physical properties of the fluid suffices to determine J and Ψ. Using the scaling law (12) for I, the droplet mean radius becomes

$$\langle R_d \rangle = h(J, \Psi) \left(\frac{\rho \varepsilon^{1/2}}{2\pi^2 \gamma^{1/2} f(\varepsilon)} \right)^{1/4} V_A^{-1/4} \left(\frac{Q^5}{K} \right)^{1/8}. \tag{49b}$$

Note that this law for $\langle R_d \rangle$ is different from both $\langle R_d \rangle \sim r_F^*$ and $\langle R \rangle_d \sim r_G^*$. The dependence of V_A on Q does not account for the disagreement, because the relatively small variations of $V_N - V_B$ observed in table 2 for a given solution and different Q are further reduced by the small exponent, 1/4, acting on V_A. The values of the jet velocity listed in table 2 support expression (49*b*). Let us write the relation between jet radius and flow rate, for a given solution, as $R_B \sim Q^x$. Then, v_B will increase with Q if $x < \frac{1}{2}$, v_B will not depend on Q if $x = \frac{1}{2}$, and v_B will increase for diminishing Q if $x > \frac{1}{2}$. We see in table 2 that, for a given solution, v_B increases when the flow rate diminishes. Thus, the exponent x in the law $R_B \sim Q^x$ must be larger than $\frac{1}{2}$. Finally, let us estimate V_A from the data listed in table 2. V_A is approximately the difference between $V_N - V_B$ and the voltage drop across the transition region, Δ, which is a fraction of $V_N - V_B$. We have already pointed out that the stopping potential of electrospray droplets for flow rates below that associated with the onset of satellite droplet is a good estimate of Δ (Gamero-Castaño 1999). The stopping potentials at low flow rates for solutions TBP1 to TBP5 are 110, 200, 340, 380 and 400 V respectively. Thus, V_A varies from approximately 500 V for TBP1 to 1200 V for TBP5.

Unfortunately, the first-order stability analysis we have carried out is only applicable to the initial stages of the jet deformation, and cannot be used to describe its complete evolution. In particular the analysis does not yield much information about the formation of satellite droplets. We observed satellite droplets in much of the electrosprays studied here. We measured the specific charge of these satellite droplets, and found it to be larger by a factor between 3 and 6 than its main droplet counterpart (see table 2). Despite its limitations, a first-order stability analysis offers some guidance about the distribution of specific charge between main and satellite droplets. The reasoning goes as follows: the volumetric charge of the main droplet will be typically the volumetric charge at the hump of the wave disturbance, while the volumetric charge of the satellite droplet is associated with the volumetric charge at the neck of the disturbance. The expression for the volumetric charge is

$$\xi = \frac{2\alpha_0}{R_0} + \varepsilon \frac{2}{R_0} (\alpha_1 - \alpha_0) \mathrm{e}^{\sigma t + \mathrm{i} k z} + O(\varepsilon^2). \tag{50}$$

When $\alpha_1 < \alpha_0$ the volumetric charge grows at the neck of the waves and decreases at the hump. If the analysis showed this ordering for α_1 and α_0 during the initial evolution of the breakup, then we could guess that the volumetric charge of satellites will be larger than that of the main droplets. The opposite holds for $\alpha_1 > \alpha_0$. Figure 17 plots the ratio α_1/α_0 as a function of the wavenumber for two electrification hypotheses, equipotential and charged bounded to surface. The third electrification case, i.e. constant volumetric charge, is not relevant because we artificially impose the volumetric charge to remain constant along the wave. Notice also that the first-order

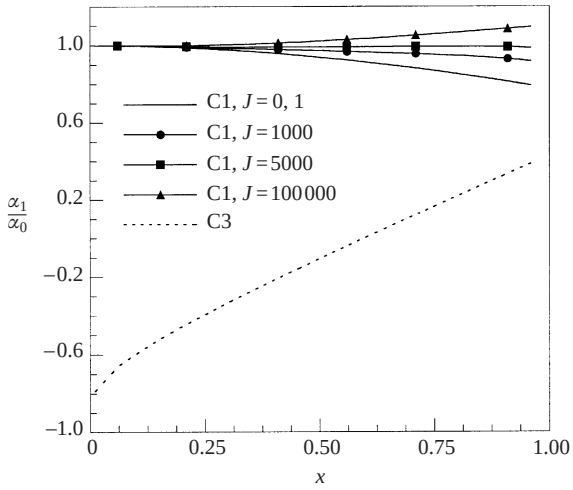

FIGURE 17. First-order term of the surface charge as a function of the wavenumber. α_1 is given in units of α_0, while the undisturbed jet radius is used to scale the wavenumber. We plot curves associated with the equipotential breakup hypothesis (C3) and the charge bounded to surface hypothesis (C1).

term of α for the case of charge bounded to the surface depends on the viscosity parameter, and hence we use several values of J to compute the α_1/α_0 curves in figure 17. From figure 17 we infer that the equipotential breakup will yield satellite droplets with a volumetric charge larger than main droplets. Only for very short wavelengths would the situation be reversed. This phenomenon might be observed using cone-jets of liquid metals with large charge parameters; it might be necessary to impose a fast enough disturbing frequency as well. More interesting is the case of charge bounded to surface, since it resembles the breakup of actual cone-jets of dielectric liquids. It is observed that for the values of the viscosity parameters characteristic of the electrosprays we have investigated, the ratio α_1/α_0 is always smaller than 1 and hence the volumetric charge of satellite droplets is expected to be larger than that of the main drops. This agrees with the experimental observations. However, it is noteworthy that for viscosity parameters larger than approximately 3000 the distribution of volumetric charge between satellite and main droplets is reversed for every distorting wavelength. Unfortunately, the observation of this surprising behaviour is likely to be difficult, since viscosity is always present and a viscosity parameter as large as 3000 is not attained in actual cone-jets (e.g. for TBP a jet with a radius of approximately 1 mm would be required). We have to point out again that the ordering of α_1 and α_0 derived from this analysis is only indicative, at most, of the direction in which the volumetric charge is redistributed between satellite and main droplets. Our analysis cannot predict the actual value of the volumetric charge in satellite droplets because it is only applicable to the initial stages of the jet deformation, and does not capture the formation of satellites.

4. Conclusions

We have used time-of-flight and energy analysis techniques to measure the voltage drop, velocity and natural wavelength for varicose breakup of the jet emerging from a Taylor cone. To the best of our knowledge, this is the first study in which any of

these parameters has been experimentally determined in charged jets of submicron radii. A large fraction of the available electrical potential is used to accelerate the charged jet. For the less-conducting solutions, the voltage drop between the electrospraying needle and the jet breakup point is as much as 90% of the voltage of the needle. The specific kinetic energy of the fluid at the breakup position is much larger than either the capillary or electric pressures. Our measurements offer a set of well defined electro-fluid-dynamic parameters in a wide range of electrospraying conditions. Other researchers working in analytical or numerical calculations of the cone-jet electrospraying mode will find these experimental parameters to be of help in modelling the problem, and ultimately, in confirming or rejecting the results from their models.

The experimental measurement of droplet diameters is unlikely to solve the question of whether the characteristic radii of the cone-jet transition region scales with $Q^{1/3}(R \sim r_F^*)$ or $Q^{1/2}(R \sim r_G^*)$. Our determination of the jet radius at the breakup point eliminates the indeterminacy associated with the formation of droplets, and is probably more accurate than previous droplet measurements. Our data coincide with Gañán's prediction for the radius of the jet (Gañán-Calvo 1997*a*). On the other hand, they also correlate well with the scaling of Fernández de la Mora & Loscertales (1994). Thus, our measurements do not provide a definitive proof for discarding either r_G^* or r_F^*.

The spread of the specific charge of the main droplets is narrower that the spread of their diameters. This experimental observation contradicts the equipotential hypothesis considered in previous calculations of the breakup of charged jets. We have extended the classical instability analysis of viscous jets to consider the effect of electric charge in varicose breakup. Three different hypotheses have been studied: breakup with electric charge bounded to the jet surface, breakup at constant volumetric charge, and an equipotential jet. Our measurements of mean radii agree tolerably well with the predictions of the breakup model, although they are not sensitive enough to decide among the three electrification hypotheses. Still, the analysis indicates that the choice of charge model influences considerably the growth rate of the disturbing waves and the natural wavelength for capillary breakup, especially for very viscous and highly charged jets ($J \lesssim 0.1$, $\Psi \gtrsim 0.3$). We find that the case of electric charge bounded to the jet surface is, of the three hypotheses, the only one that explains the experimental observations regarding the invariance of specific charge among main droplets and the increased specific charge of satellite droplets. We anticipate that choosing the right electrification hypothesis is paramount to investigating the effect of charge on capillary breakup, especially for more elaborate nonlinear models in which parameters such as the distribution of charge between main and satellite droplets are sought.

The effect of viscosity on the jet breakup is most important for moderately and highly conducting solutions ($K \gtrsim 10^{-3}\,\mathrm{S\,m^{-1}}$), and/or very viscous liquids. In this limit, the common practice of using the inviscid value of 1.89 for the ratio between droplet and jet diameters leads to important errors.

We are indebted to Professors Fernández de la Mora (Yale University) and Martínez-Sánchez (Massachusetts Institute of Technology) for numerous discussions on the subject. Many ideas regarding the interpretation and analysis of the stopping-potential and time-of-flight curves originated in discussions between M.G.C. and Fernández de la Mora. This research is supported by a NASA Phase II SBIR contract. We acknowledge gratefully the support given by Mr J. Sovey, the NASA technical monitor of this contract.

REFERENCES

Aris, R. 1989 *Vectors, Tensors, and the Basic Equations of Fluid Mechanics*, p. 231. Dover.

Chandrasekhar, S. 1981 *Hydrodynamic and Hydromagnetic Stability*, pp. 515–576. Dover.

Chen, D. R. & Pui, D. 1997 Experimental investigation of scaling laws for electrospraying: dielectric constant effect. *Aerosol Sci. Technol.* **27**, 367–380.

Chen, D. R., Pui, D. & Kaufman, S. 1995 Electrospraying of conducting liquids for monodisperse aerosol generation in the 4 nm to 1.8 μm diameter range. *J. Aerosol Sci.* **26**, 963–977.

Cherney, L. 1999 Structure of Taylor cone-jets. Limit of low flow rates. *J. Fluid Mech.* **378**, 167–196.

Cloupeau, M. & Prunet-Foch, B. 1990 Electrostatic spraying of liquids: main functioning mode. *J. Electrostat.* **25**, 165–184.

Fenn, J. B., Mann, M., Meng, C. K., Wong, S. K. & Whitehouse, C. 1989 Electrospray ionization for mass spectrometry of large biomolecules. *Science* **246**, 64–71.

Fernández de la Mora, J. 1996 On the outcome of the Coulombic fission of a charged isolated drop. *J. Colloid Interface Sci.* **178**, 209–218.

Fernández de la Mora, J. & Loscertales, I. G. 1994 The current emitted by highly conducting Taylor cones. *J. Fluid Mech.* **260**, 155–184.

Fuerstenau, S. & Benner, W. H. 1995 Molecular weight determination of megadalton DNA electrospray ions using charge detection time-of flight spectrometry. *Rapid Commun. Mass Spec.* **15**, 1528–1538.

Gamero-Castaño, M. 1999 The transfer of ions and charged nanoparticles from solution to the gas phase in electrosprays. PhD Thesis, Yale University.

Gañán-Calvo, A. M. 1997*a* Cone-jet analytical extension of Taylor's electrostatic solution and the asymptotic universal scaling laws in electrospraying. *Phys. Rev. Lett.* **79**, 217–220.

Gañán-Calvo, A. M. 1997*b* On the theory of electrohydrodynamically driven capillary jets. *J. Fluid Mech.* **335**, 165–188.

Gañán-Calvo, A. M., Dávila, J. & Barrero, A. 1997 Current and droplet size in the electrospraying of liquids. Scaling laws. *J. Aerosol Sci.* **28**, 249–275.

Gamero-Castaño, M. & Fernández de la Mora, J. 2000 Direct measurement of ion evaporation kinetics from electrified liquid surfaces. *J. Chem. Phys.* **113**, 815–832.

Gamero-Castaño, M. & Hruby, V. 2001 Electrospray as a source of nanoparticles for efficient colloid thrusters. *J. Propulsion Power* **17**, 977–987.

Hartman, R. P. A., Brunner, D. J., Camelot, D. M. A., Marijnissen, J. C. M. & Scarlett, B. 2000 Jet break-up in electrohydrodynamic atomization in the cone-jet mode. *J. Aerosol Sci.* **31**, 65–95.

Hogan, J. J. & Hendricks, C. D. 1965 Investigation of the charge-to-mass ratio of electrically sprayed liquid particles. *AIAA J.* **3**, 296–301.

Huberman, M. N. & Rosen, S. G. 1974 Advanced high-thrust colloid sources. *J. Spacecraft* **11**, 475–480.

Javorek, A. & Krupa, A. 1996 Generation and characteristics of the precession mode of EHD spraying. *J. Aerosol Sci.* **27**, 75–82.

De Juan, L. & Fernández de la Mora, J. 1997 Charge and size distribution of electrospray drops. *J. Colloid. Interface Sci.* **186**, 280–293.

Lenggoro, I. W., Okuyama, K., Fernández de la Mora, J. & Tohge, N. 2000 Preparation of ZnS nanoparticles by electrospray pyrolysis. *J. Aerosol Sci.* **31**, 121–136.

López-Herrera, J. M., Gañán-Calvo, A. M. & Pérez-Saborid, M. 1999 One-dimensional simulation of the breakup of capillary jets of conducting liquids. Application to E.H.D. spraying. *J. Aerosol Sci.* **30**, 895–912.

Mestel, A. J. 1994 Electrohydrodynamic stability of a slightly viscous jet. *J. Fluid Mech.* **274**, 93–113.

Mestel, A. J. 1996 Electrohydrodynamic stability of a highly viscous jet. *J. Fluid Mech.* **312**, 311–326.

Rayleigh, Lord 1945 *Theory of Sound*, Dover, pp. 357–364.

Riddick, J. A., Bunger, W. B. & Sakano, T. K. 1986 *Organic Solvents. Physical Properties and Methods of Purification*, 4th Edn. Wiley.

Rosell-Llompart, J. & Fernández de la Mora, J. 1994 Generation of monodisperse droplets 0.3 to 4 mm in diameter from electrified cone-jets of highly conducting and viscous liquids. *J. Aerosol Sci.* **25**, 1093–1119.

Saville, D. A. 1971*a* Stability of electrically charged viscous cylinders. *Phys. Fluids* **14**, 1095–1099.

Saville, D. A. 1971*b* Electrohydrodynamic stability: effects of charge relaxation at the interface of a liquid jet. *J. Fluid Mech.* **48**, 815–827.

Saville, D. A. 1997 Electrohydrodynamics: the Taylor–Melcher leaky dielectric model. *Annu. Rev. Fluid Mech.* **29**, 27–64.

Tang, K. & Gomez, A. 1994 On the structure of an electrostatic spray of monodisperse droplets. *Phys. Fluids* **6**, 2317–2332.